Science Advances
AAAS

Supplementary Materials for

Cryo-EM structure and electrophysiological characterization of ALMT from *Glycine max* reveal a previously uncharacterized class of anion channels

Li Qin, Ling-hui Tang, Jia-shu Xu, Xian-hui Zhang, Yun Zhu, Chun-rui Zhang, Mei-hua Wang, Xue-lei Liu, Fei Li, Fei Sun, Min Su*, Yujia Zhai*, Yu-hang Chen*

*Corresponding author. Email: yuhang.chen@genetics.ac.cn (Y.-h.C.); yujia@ibp.ac.cn (Y. Zhai); minsu@genetics.ac.cn (M.S.)

Published 2 March 2022, *Sci. Adv.* **8**, eabm3238 (2022)
DOI: 10.1126/sciadv.abm3238

The PDF file includes:

Other Supplementary Material for this manuscript includes the following:

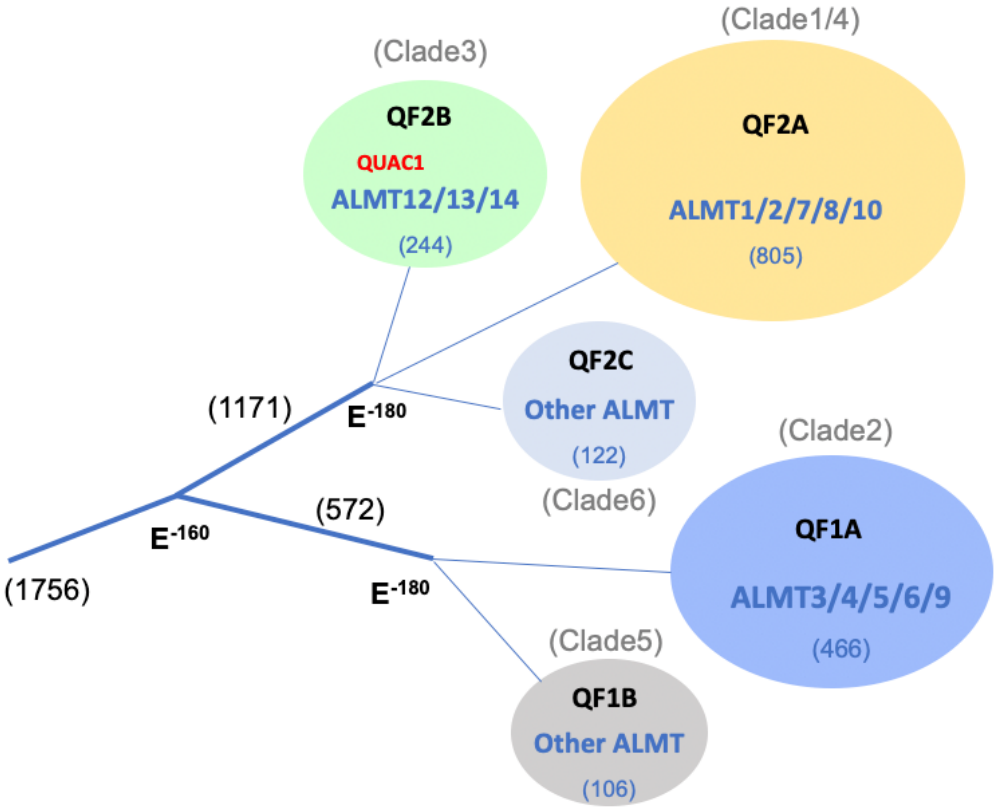

Fig. S1. Family tree of the ALMT/QUACs.

The presentation was computed by the program COBALT from representative sequences, including thirteen *Arabidopsis* ALMTs, and two other ALMTs. The clustering of sequences into a subfamily was performed using PSI-BLAST at the different levels ($E \leq 10^{-160}$, $E \leq 10^{-180}$) with representative sequences, as detailed in the table S1. The numbers of the sequences in the family/subfamily are indicated in parentheses. The clade numbering in previous work (*60*) is also indicated, and the Clade6 is a new group.

60. I. Dreyer, J. L. Gomez-Porras, D. M. Riaño-Pachón, R. Hedrich, D. Geiger, Molecular evolution of slow and quick anion channels (SLACs and QUACs/ALMTs). *Front. Plant Sci.* **3**, 1–12 (2012).

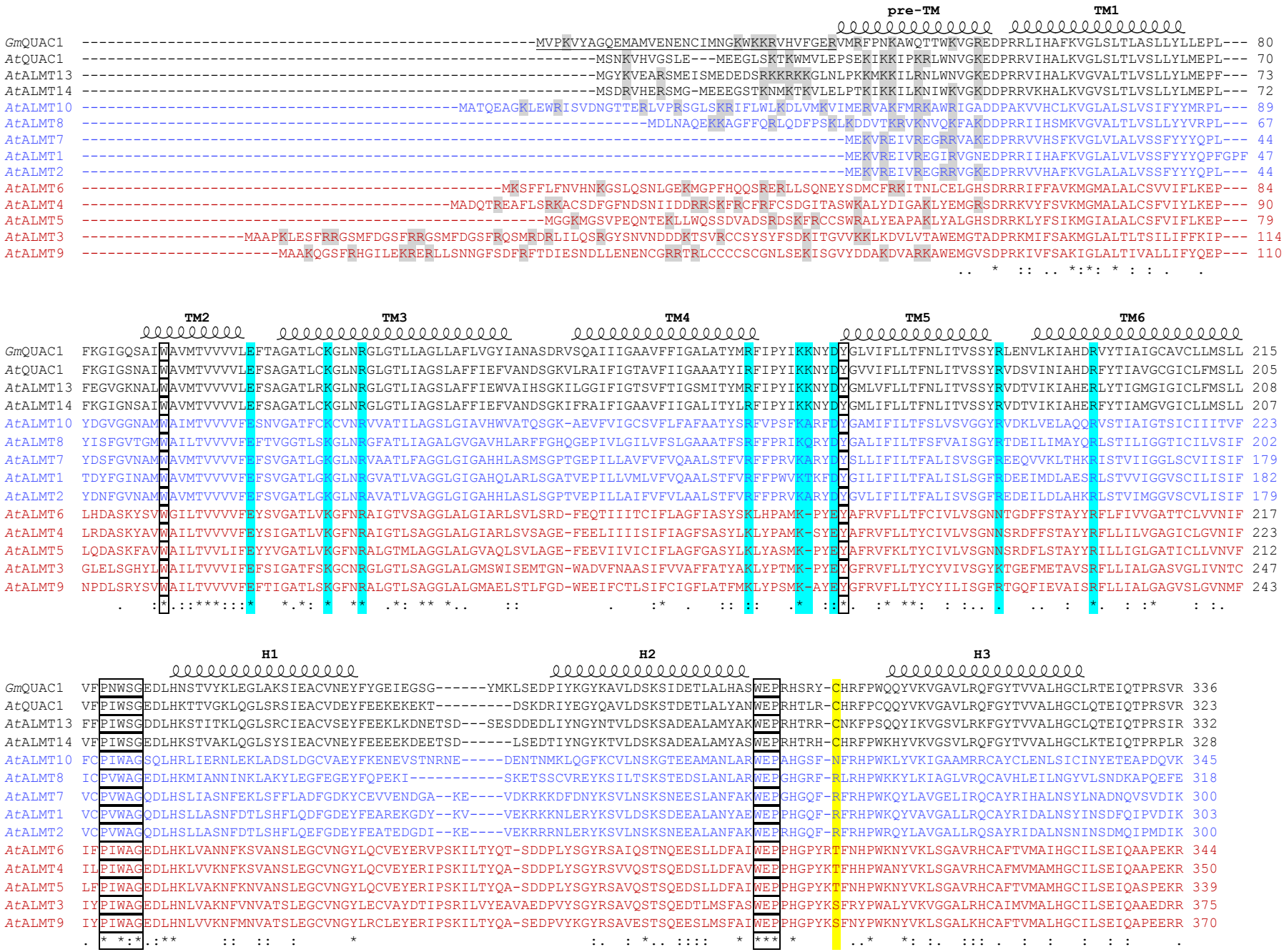
pre-TM
TM1
TM2
TM3
TM4
TM5
TM6
H1
H2
H3
GmQUAC1
AtQUAC1
AtALMT13
AtALMT14
AtALMT10
AtALMT8
AtALMT7
AtALMT1
AtALMT2
AtALMT6
AtALMT4
AtALMT5
AtALMT3
AtALMT9

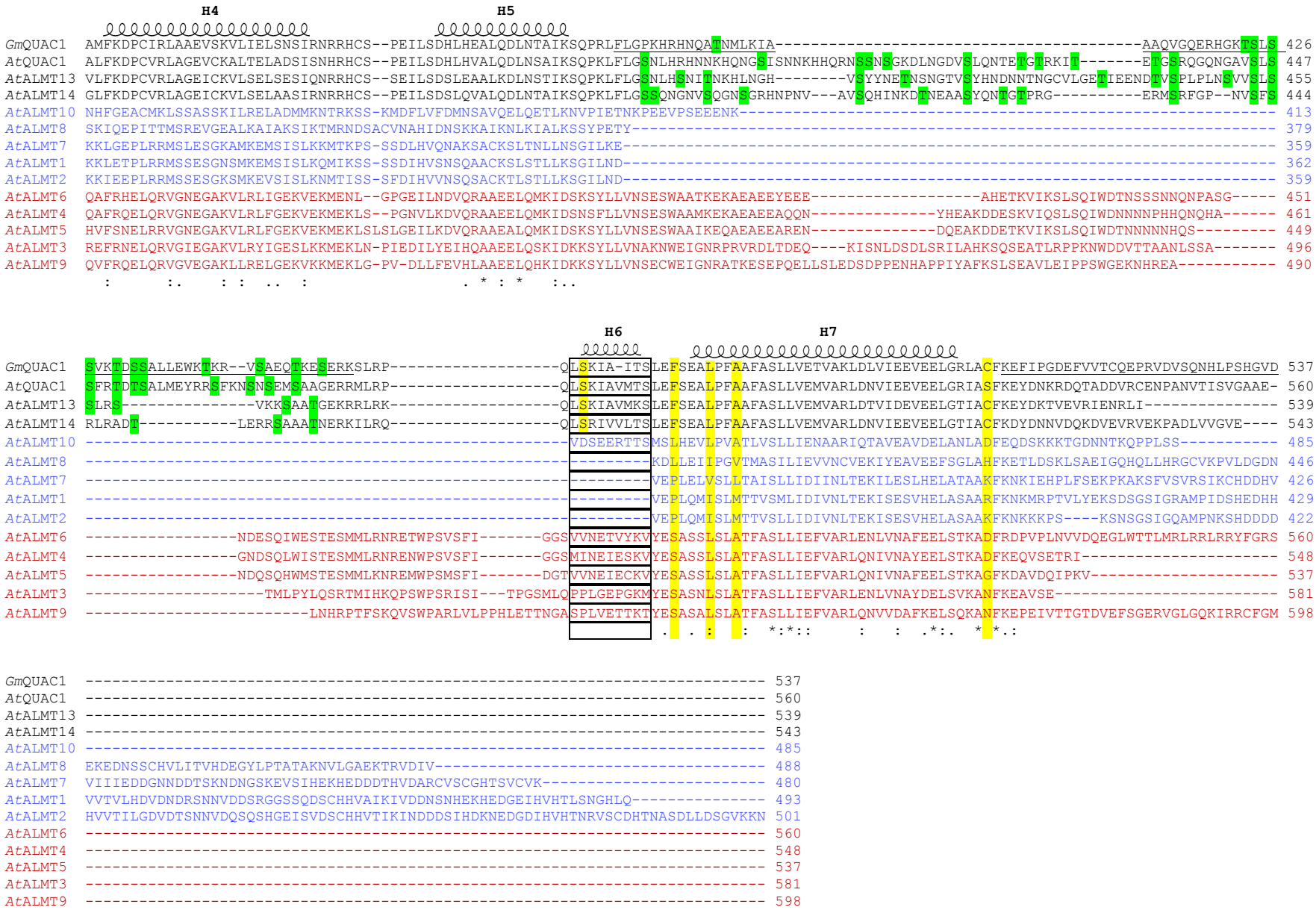

Fig. S2. Structure-based sequence alignment for plant ALMT/QUACs.

Structure-based sequence alignments of thirteen *Arabidopsis* ALMT/QUACs and *Gm*ALMT12/QUAC1. The structure of *Gm*ALMT12/QUAC1 has been used to restrict sequence gaps to inter-helical segments, with the superior coils defining extents of the helical segments. The disordered regions in *Gm*ALMT12/QUAC1 (residues 1-35, 394-454 and 507-537) are indicated by underlines. The aligned sequences are as following: *Gm*ALMT12/QUAC1 (XP_003516635.1), *At*ALMT12/QUAC1 (NP_193531.1), *At*ALMT1 (NP_172319.1), *At*ALMT2 (NP_172320.1), *At*ALMT3 (NP_173278.1), *At*ALMT4 (NP_173919.1), *At*ALMT5(NP_564935.1), *At*ALMT6 (NP_179338.1), *At*ALMT7 (NP_001324626.1), *At*ALMT8 (NP_187774.1), *At*ALMT9 (NP_188473.1), *At*ALMT10 (NP_001319836.1), *At*ALMT13 (NP_199472.1), *At*ALMT14 (NP_199473.1).

The protein sequences are from three major groups: QF1A (*At*ALMT3/4/5/6/9) in red; QF2A (*At*ALMT1/2/7/8/10) in blue; QF2B (*Gm*ALMT12/QUAC1, *At*ALMT12/13/14) in black. Overall, the protein sequences in the QF2A have a shorter pre-TM region, and lack a disordered region and a domain-swapped helix found in the *Gm*ALMT12/QUAC1 structure.

Some key residues are highlighted or indicated as following:

1. The pore-lining positively charged R/K residues are highlighted in cyan (K109/R113/R158/K164/K165/R187/R198 in *Gm*ALMT12/QUAC1), and related interacting negatively-charged E/D residues are also highlighted in cyan (E100/D168 in *Gm*ALMT12/QUAC1).
2. The residues of mutagenesis for disrupting dimer interaction are highlighted in yellow (S461/F470/L474/A477 in *Gm*ALMT12/QUAC1).
3. Positively charged residues at the N-terminal pre-TM juxtamembrane helix are highlighted in grey.
4. Potential phosphorylation sites in the disordered regions of C-terminal CHD are highlighted in green.
5. The domain-swapped helix regions are indicated in a box (helix H6 in *Gm*ALMT12/QUAC1).
6. Other conserved motifs are indicated in boxes (W90, Y169, P218-N219-W220-S221-G222 and W288-E289-P290 in *Gm*ALMT12/QUAC1).

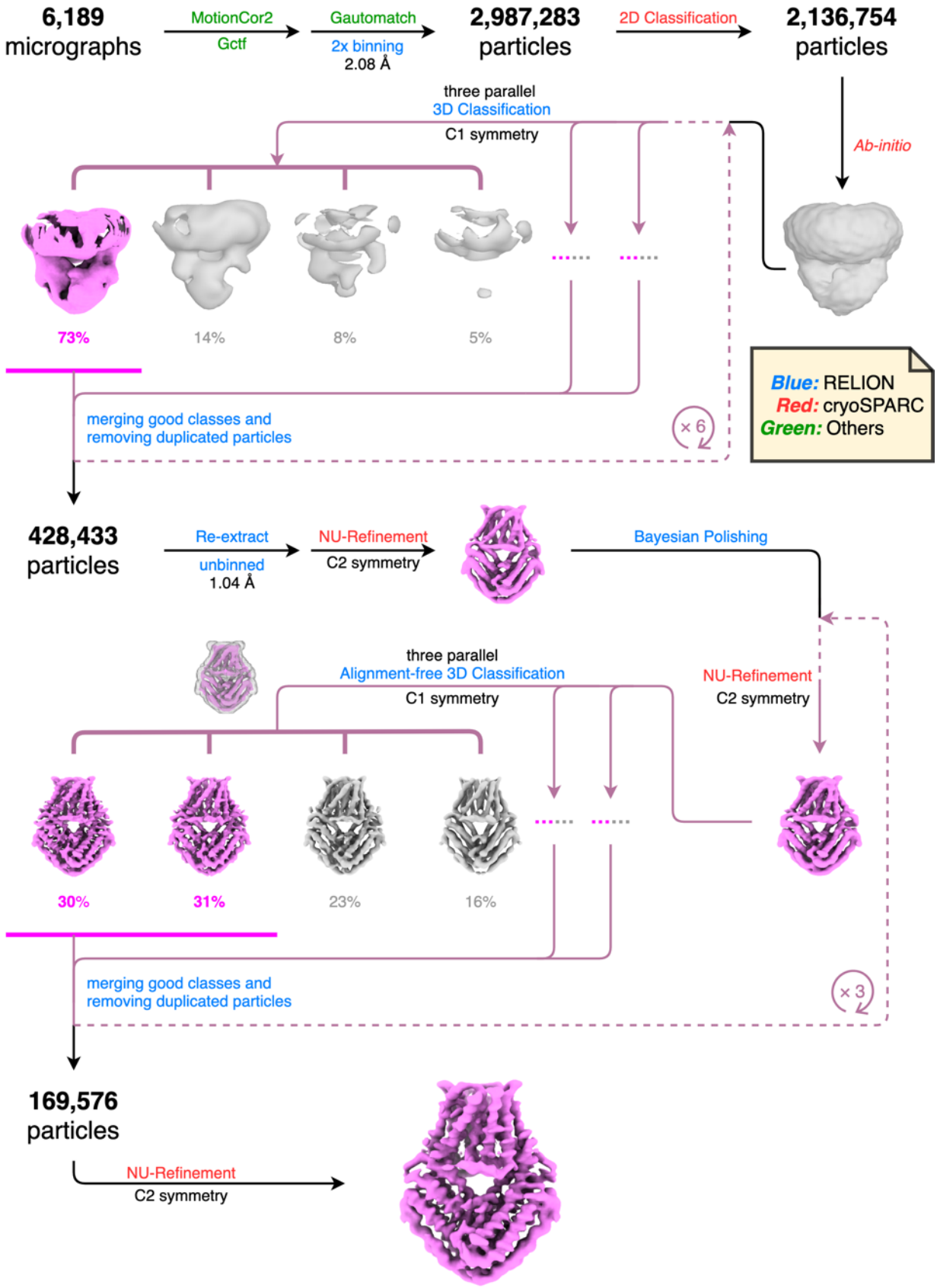

Fig. S3. The workflow for image processing of *Gm*ALMT12/QUAC1.

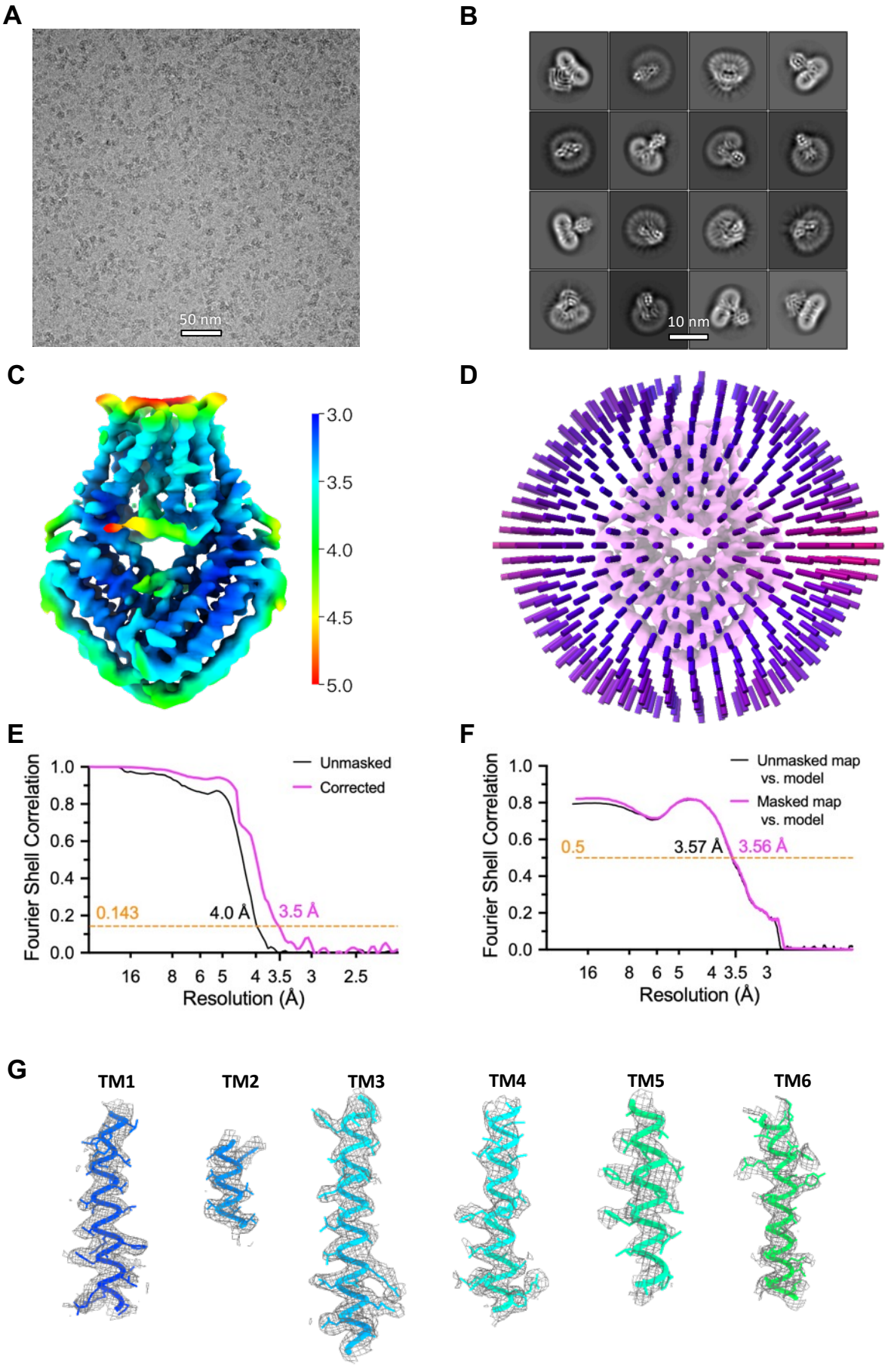

Fig. S4. Cryo-EM analysis of *Gm*ALMT12/QUAC1.

(**A**) Representative micrograph of *Gm*ALMT12/QUAC1.

(**B**) Representative 2D class averages of *Gm*ALMT12/QUAC1.

(**C**) Local resolution electron density map of *Gm*ALMT12/QUAC1.

(**D**) Euler angle distribution plot of particle projections in reconstruction of *Gm*ALMT12/QUAC1.

(**E**) Fourier shell correlation (FSC) curve suggests an overall resolution at 3.5 Å, as estimated using the 0.143 cut-off criterion (dotted line).

(**F**) Cross-validation of model to cryo-EM density map suggests a resolution at 3.5 Å, as estimated using the 0.5 cut-off criterion (dotted line). All line charts in (E) and (F) were prepared in GraphPad Prism.

(**G**) Representative cryo-EM density map for the TM segments.

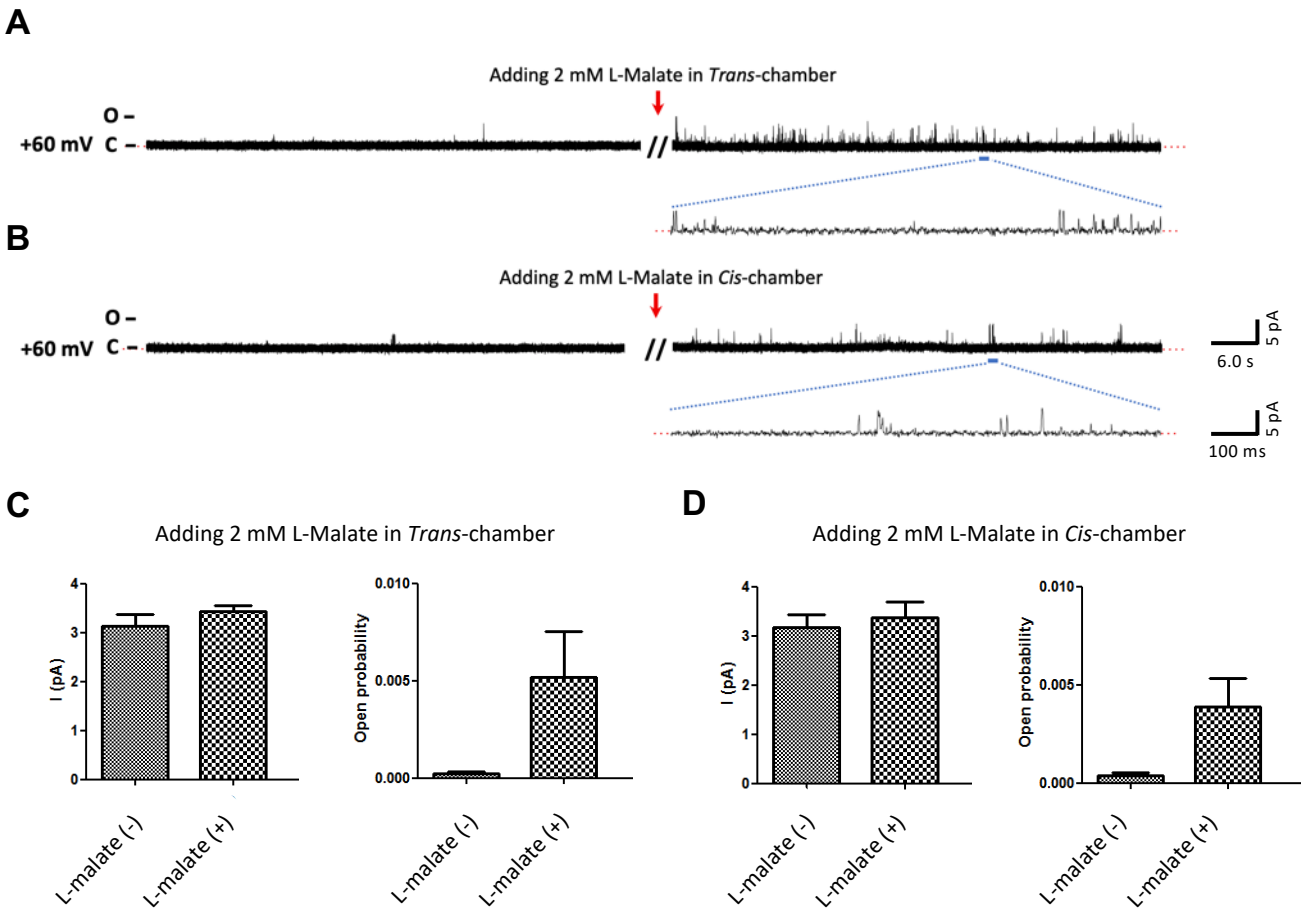

Fig. S5. Single channel analysis of malate regulation on *Gm*ALMT12/QUAC1.

(**A** and **B**) The representative current traces at +60 mV, before and after adding 2 mM L-malate to the *trans*- (A) or *cis*- (B) chamber. The chambers were filled with symmetrical solutions of 150 mM NaCl, and the purified *Gm*ALMT12/QUAC1^{NaCl} proteins were added to the *cis*-side.

(**C** and **D**) The regulation effect of malate on the *Gm*ALMT12/QUAC1^{NaCl} in the NaCl solutions. The current amplitude (left) and open probability (right) analysis for the recordings, before (–) or after (+) addition of 2 mM L-malate to the *trans*- (C) or *cis*- (D) chamber, are shown (Data are mean ± SEM, n=3 for each group).

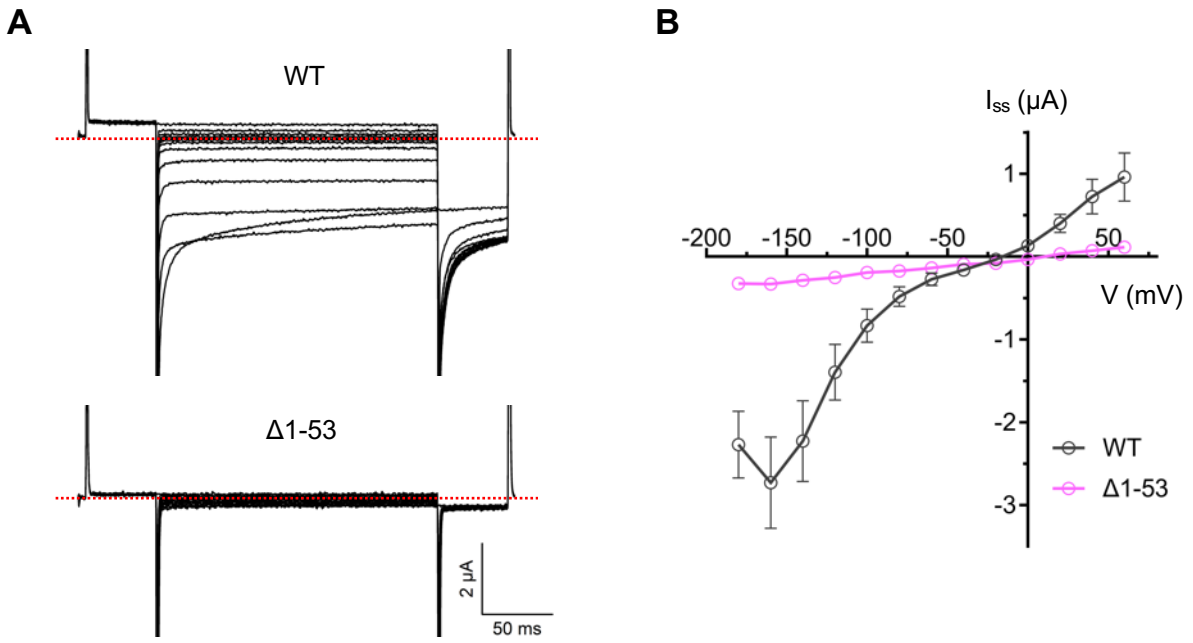

Fig. S6. Analyses of the *Gm*ALMT12/QUAC1 pre-TM helix deletion mutant by TEVC recording.

(**A**) Representative current traces recorded at different voltages (from +60 mV to –180 mV in 20 mV decrement) in the external solutions of 30 mM L-malate for the *Gm*ALMT12/QUAC1 wild-type (upper) and Δ1-53 mutant (lower).

(**B**) Steady-state current-voltage (I_{ss}-V) relations of the *Gm*ALMT12/QUAC1 wild-type and Δ1-53 mutant (Data are mean ± SEM, n≥6).

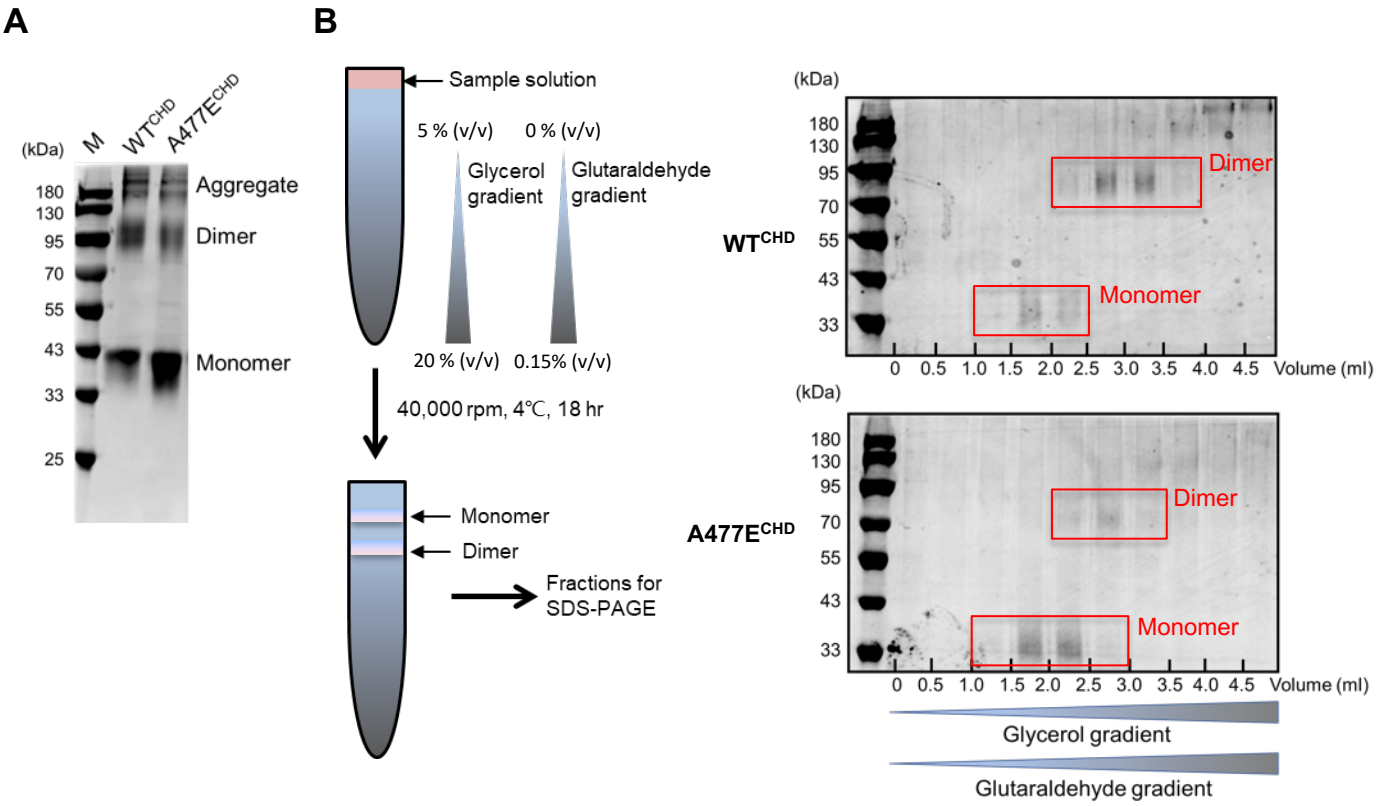

Fig. S7. Cross-linking experiments of the CHD proteins.

(**A**) Cross-linking of purified CHD proteins, wild-type (WT^{CHD}) and A477E mutant ($A477E^{CHD}$). Equal amount of proteins were incubated with 0.01% glutaraldehyde at 4℃ for 3 hr. The reactions were quenched with 50 mM Tris-HCl (pH 8.0), and analyzed by 10% SDS-PAGE.

(**B**) Gradient fixation (GraFix) of the purified WT^{CHD} and $A477E^{CHD}$ proteins. Equal amount of proteins were loaded onto the gradient of glycerol and glutaraldehyde, and ultra-centrifuged at 40,000 rpm, 4℃ for 18 hr. The fractions of 0.5 ml were collected, and quenched with a final concentration of 80 mM glycine. The fractions were analyzed by 10% SDS-PAGE. In both experiments, the wild-type CHD results in more cross-linked dimer than that of A477E mutant under parallel conditions.

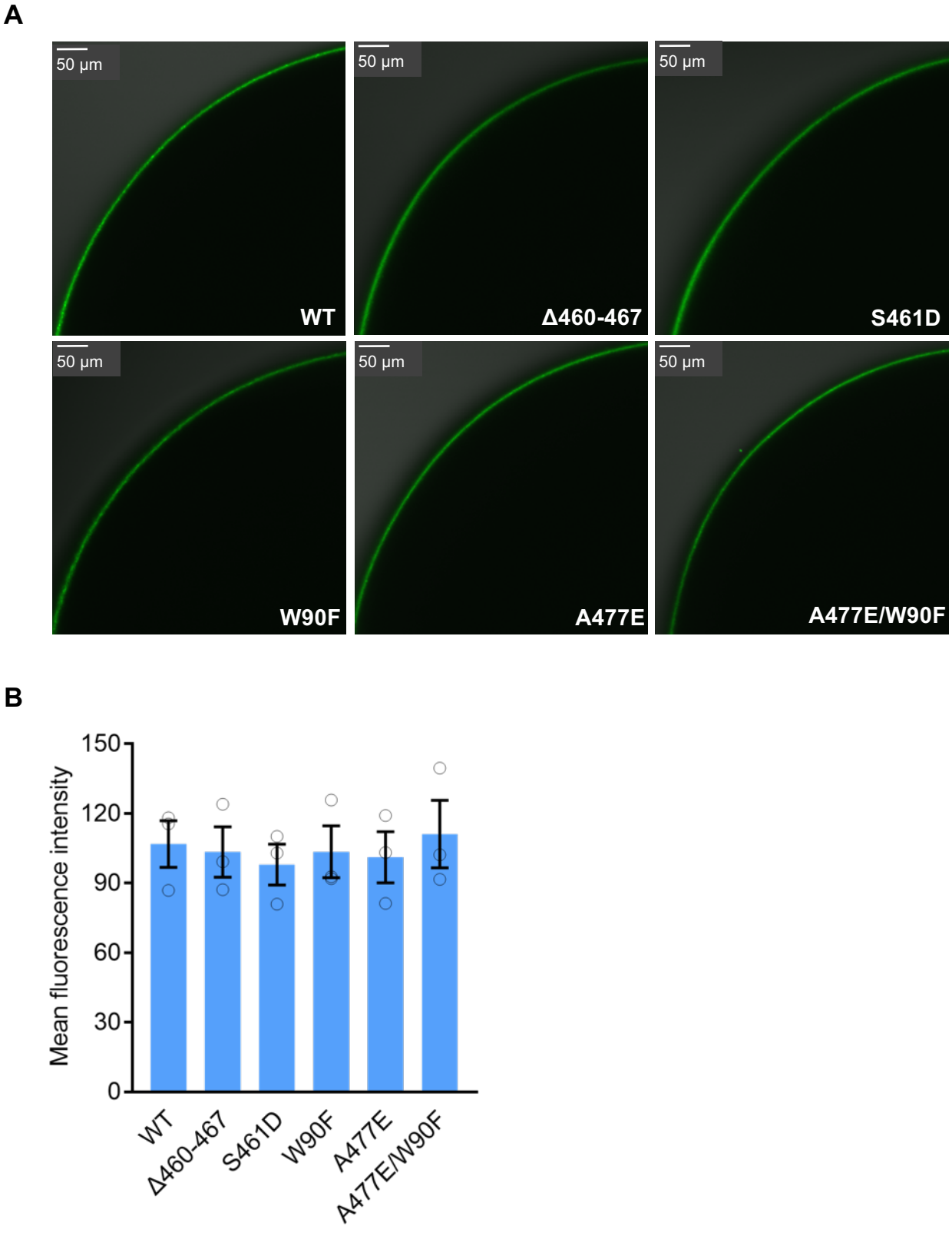

Fig. S8. Fluorescence and confocal imaging of the C-terminal GFP tagged *Gm*ALMT12/QUAC1.

(**A**) Representative fluorescence images of *Gm*ALMT12/QUAC1 wild-type (WT) and mutants (Δ460-467, S461D, W90F, A477E and A477E/W90F). The cRNAs fused with C-terminal GFP were injected into the *Xenopus laevis* oocytes. After ~48 hr expression at 18°C, the GFP fluorescence on the plasma membrane of oocytes was analyzed by a laser confocal microscope.

(**B**) Mean fluorescence intensity measurements by using software ImageJ. A one-way ANOVA analysis was performed with a P value of 0.9704, showing no significant differences between them. (Data are mean ± SEM, n=3).

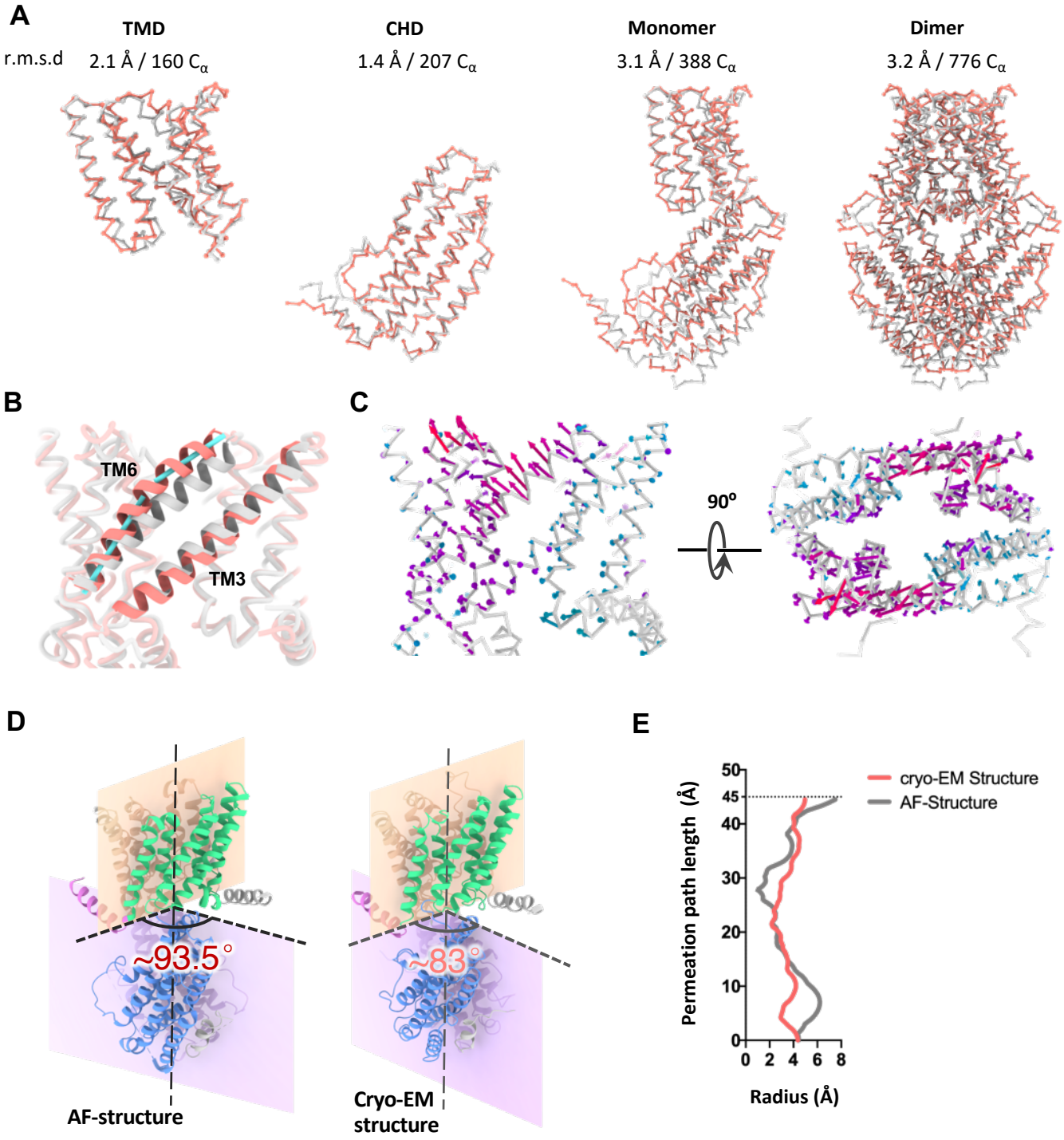

Fig. S9. Comparison of the cryo-EM structure and AF-structure.

(**A**) Superimposition of the cryo-EM structure (salmon) and AF-structure (grey). The superimposed Cα and their r.m.s.d values are indicated.

(**B**) The comparison of the cryo-EM structure (salmon) and AF-structure (grey). The TM3 and TM6 helices are shown in cartoon.

(**C**) The porcupine plot showing the motion across the AF-structure and the cryo-EM structure. The arrows indicate direction of motion and magnitude of the movements of the Cα positions (from the AF-structure to the cryo-EM structure). The Cα traces for the AF-structure are shown. The colors for the arrows are indicated as followings: red (outward motion), green (inward motion) and blue (static).

(**D**) The dihedral angle between the TMD and CHD interfaces in the AF-structure and the cryo-EM structure are 93.5º and 83º, respectively. The 10.5º rotation between these two states suggests that domain rearrangement occurs during conformational conversion. We speculate that the domain re-organization is coupled to channel gating.

(**E**) Plot of the pore radius as a function of the pore axis, cryo-EM structure (salmon) *vs.* AF-structure (grey).

Table S1

PSI-BLAST analysis of ALMT/QUAC -related proteins[a]

Family /Subfamily	Representative expansion sequence	GenBank ID	-log(E_{cut})	Sequence
QF1	*Arabidopsis thaliana* ALMT9	NP_188473.1	160	572
QF2	*Arabidopsis thaliana* ALMT2	NP_172320.1	160	1171
Others[b]				13
Total				1756
QF1A	*Arabidopsis thaliana* ALMT9	NP_188473.1	180	466
QF1B	*Oryza sativa Japonica* ALMT9	XP_015618041.1	180	106
Sub-total				572
QF2A	*Arabidopsis thaliana* ALMT2	NP_172320.1	180	805
QF2B[c]	*Arabidopsis thaliana* ALMT12/QUAC1	NP_193531.1	180	244
QF2C	*Helianthus annuus* ALMT4	XP_022041099.1	180	122
Sub-total				1171

[a] Procedures for the PSI-BLAST analysis of the ALMT/QUAC superfamily:

- NCBI PSI-BLAST: Thirteen expansion sequences used to define the ALMT/QUAC superfamily were as following: *At*ALMT12/QUAC1 (NP_193531.1), *At*ALMT1 (NP_172319.1), *At*ALMT2 (NP_172320.1), *At*ALMT3 (NP_173278.1), *At*ALMT4 (NP_173919.1), *At*ALMT5(NP_564935.1), *At*ALMT6 (NP_179338.1), *At*ALMT7 (NP_001324626.1), *At*ALMT8 (NP_187774.1), *At*ALMT9 (NP_188473.1), *At*ALMT10 (NP_001319836.1), *At*ALMT13 (NP_199472.1) and *At*ALMT14 (NP_199473.1). The *At*ALMT11 was not included, as it has only 152 amino acid in length, containing less than 6 TM and lacking the putative C-terminal helical domain.

The expansion sequences were run against the NCBI Protein Reference Sequence (refseq_protein), in which the green plants (taxid:33090) and an E-value $\leq 5\times10^{-3}$ were selected. Each sequence reached convergence at the 4th or 5th PSI-BLAST run, having generated ~2000 sequences. The resulted thirteen pools were merged to obtain a non-redundant set (2,061 sequences), to which some further purification was applied: i) removal of sequences not having a starting Met or containing non-amino acid X; ii) removal of sequences containing keyword “partial” in the sequence annotation; iii) removal of sequences <400 residues, unless 6 transmembrane segments confirmed by TMHMM 2.0. This resulted in a set of 1,843 sequences, which were subjected to the prediction of TM segments using THHMM 2.0. The sequences with fewer than 5 apparent TM helices were checked by *Gm*ALMT12/QUAC1 structure-based multiple sequence alignment with CLUSTAL_W, and sequences obviously lacking some TM helices, or having deletion/insertion in the middle of TM or other helix in the C-terminal domain were removed. This reduced to a final pool of 1,756 sequences for family/subfamily classification.

- Local PSI-BLAST:

The 1,756 identified sequences were used to establish a local PSI-BLAST database into which various sequences were expanded at different E_{cut} levels. We found that at $E_{cut} = 10^{-160,}$ there were two distinct families plus several others. And subfamilies were divided at the level of $E_{cut} = 10^{-180}$.

[b]The other leftover sequences include 9 from *Physcomitrium patens*, 3 from *Selaginella moellendorffii*, and 1 from *Chlorella variabilis*.

[c]In QF2B, after removing redundant sequence >95% sequence identity, a set of 155 sequences was achieved. We further checked the sequences by *Gm*ALMT12/QUAC1 structure-based multiple sequence alignment with CLUSTAL_W, and sequences obviously lacking some TM helix, or having deletion/insertion in the TM or helices in the C-terminal domain were removed. A final set of 137 sequences was achieved and used for sequence conservation analysis in Fig. 3C.

Table S2
Statistics of data colletion, image processing and model building

Sample	*Gm*ALMT12/QUAC1
PDB	7W6K
EMDB	EMD-32328
Data Collection	
Microscope	Titan Krios G2
Voltage [kV]	300
Dectector	Gatan K2 Summit
Energy filter width [eV]	20
Automation software	SerialEM
Pixel size [Å/pixel]	1.04
Electron dose [$e^-/Å^2$]	60
No. of frames	32
Defocus range [μm]	-1.2 ~ -2.2
Reconstruction	
Software	cryoSPARC 3.1 & Relion 3.0
No. of particles	169,576
Symmetry	C2
Map sharpening B-factor[$Å^2$]	189
Final resolution [Å]	3.5
Model Building & Refinement	
Building Software	Coot
Refinement Software	PHENIX
Rmsd (bond) [Å]	0.005
Rmsd (angle) [°]	0.692
MolProbity score	2.36
Model Compesition	
No. of residues	820
Ligands	None
Validation	
Ramachandran plot[%]	
Outliers	0
Allowed	9.5
Favored	90.5
Rotamer Outliers [%]	2.01

REFERENCES AND NOTES

1. S. Meyer, J. Scholz-Starke, A. De Angeli, P. Kovermann, B. Burla, F. Gambale, E. Martinoia, Malate transport by the vacuolar *At*ALMT6 channel in guard cells is subject to multiple regulation. *Plant J.* **67**, 247–257 (2011).

2. S. Meyer, P. Mumm, D. Imes, A. Endler, B. Weder, K. A. S. Al-Rasheid, D. Geiger, I. Marten, E. Martinoia, R. Hedrich, *At*ALMT12 represents an R-type anion channel required for stomatal movement in *Arabidopsis* guard cells. *Plant J.* **63**, 1054–1062 (2010).

3. T. Sasaki, I. C. Mori, T. Furuichi, S. Munemasa, K. Toyooka, K. Matsuoka, Y. Murata, Y. Yamamoto, Closing plant stomata requires a homolog of an aluminum-activated malate transporter. *Plant Cell Physiol.* **51**, 354–365 (2010).

4. A. De Angeli, J. Zhang, S. Meyer, E. Martinoia, *At*ALMT9 is a malate-activated vacuolar chloride channel required for stomatal opening in *Arabidopsis*. *Nat. Commun.* **4**, 1804 (2013).

5. P. Kovermann, S. Meyer, S. Hörtensteiner, C. Picco, J. Scholz-Starke, S. Ravera, Y. Lee, E. Martinoia, The *Arabidopsis* vacuolar malate channel is a member of the ALMT family. *Plant J.* **52**, 1169–1180 (2007).

6. T. Gutermuth, S. Herbell, R. Lassig, M. Brosché, T. Romeis, J. A. Feijó, R. Hedrich, K. R. Konrad, Tip-localized Ca^{2+}-permeable channels control pollen tube growth via kinase-dependent R- and S-type anion channel regulation. *New Phytol.* **218**, 1089–1105 (2018).

7. S. Herbell, T. Gutermuth, K. R. Konrad, An interconnection between tip-focused Ca^{2+} and anion homeostasis controls pollen tube growth. *Plant Signal. Behav.* **13**, e1529521 (2018).

8. T. Sasaki, Y. Yamamoto, B. Ezaki, M. Katsuhara, S. J. Ahn, P. R. Ryan, E. Delhaize, H. Matsumoto, A wheat gene encoding an aluminum-activated malate transporter. *Plant J.* **37**, 645–653 (2004).

9. O. A. Hoekenga, L. G. Maron, M. A. Piñeros, G. M. A. Cançado, J. Shaff, Y. Kobayashi, P. R. Ryan, B. Dong, E. Delhaize, T. Sasaki, H. Matsumoto, Y. Yamamoto, H. Koyama, L. V. Kochian, *AtALMT1*, which encodes a malate transporter, is identified as one of several genes critical for aluminum tolerance in *Arabidopsis*. *Proc. Natl. Acad. Sci. U.S.A.* **103**, 9738–9743 (2006).

10. A. Ligaba, L. Maron, J. Shaff, L. Kochian, M. Piñeros, Maize *Zm*ALMT2 is a root anion transporter that mediates constitutive root malate efflux. *Plant Cell Environ.* **35**, 1185–1200 (2012).

11. A. De Angeli, U. Baetz, R. Francisco, J. Zhang, M. M. Chaves, A. Regalado, The vacuolar channel *Vv*ALMT9 mediates malate and tartrate accumulation in berries of *Vitis vinifera*. *Planta* **238**, 283–291 (2013).

12. T. Rudrappa, K. J. Czymmek, P. W. Paré, H. P. Bais, Root-secreted malic acid recruits beneficial soil bacteria. *Plant Physiol.* **148**, 1547–1556 (2008).

13. S. A. Ramesh, S. D. Tyerman, B. Xu, J. Bose, S. Kaur, V. Conn, P. Domingos, S. Ullah, S. Wege, S. Shabala, J. A. Feijó, P. R. Ryan, M. Gillham, GABA signalling modulates plant growth by directly regulating the activity of plant-specific anion transporters. *Nat. Commun.* **6**, 7879 (2015).

14. H. Zhang, Y. Li, J. K. Zhu, Developing naturally stress-resistant crops for a sustainable agriculture. *Nat. Plants*. **4**, 989–996 (2018).

15. B. U. Keller, R. Hedrich, K. Raschke, Voltage-dependent anion channels in the plasma membrane of guard cells. *Nature* **341**, 450–453 (1989).

16. P. Dietrich, R. Hedrich, Interconversion of fast and slow gating modes of GCAC1, a Guard Cell Anion Channel. *Planta* **195**, 301–304 (1994).

17. J. I. Schroeder, B. U. Keller, Two types of anion channel currents in guard cells with distinct voltage regulation. *Proc. Natl. Acad. Sci. U.S.A.* **89**, 5025–5029 (1992).

18. P. Mumm, D. Imes, E. Martinoia, K. A. S. Al-Rasheid, D. Geiger, I. Marten, R. Hedrich, C-terminus-mediated voltage gating of *Arabidopsis* guard cell anion channel QUAC1. *Mol. Plant* **6**, 1550–1563 (2013).

19. R. Hedrich, I. Marten, G. Lohse, P. Dietrich, H. Winter, G. Lohaus, H.-W. Heldt, Malate-sensitive anion channels enable guard cells to sense changes in the ambient CO_2 concentration. *Plant J.* **6**, 741–748 (1994).

20. K. Raschke, Alternation of the slow with the quick anion conductance in whole guard cells effected by external malate. *Planta* **217**, 651–657 (2003).

21. D. Imes, P. Mumm, J. Böhm, K. A. S. Al-Rasheid, I. Marten, D. Geiger, R. Hedrich, Open stomata 1 (OST1) kinase controls R-type anion channel QUAC1 in *Arabidopsis* guard cells. *Plant J.* **74**, 372–382 (2013).

22. K. Luu, N. Rajagopalan, J. C. H. Ching, M. C. Loewen, M. E. Loewen, The malate-activated ALMT12 anion channel in the grass *Brachypodium distachyon* is co-activated by Ca^{2+}/calmodulin. *J. Biol. Chem.* **294**, 6142–6156 (2019).

23. L. Holm, DALI and the persistence of protein shape. *Protein Sci.* **29**, 128–140 (2020).

24. T. Furuichi, T. Sasaki, Y. Tsuchiya, P. R. Ryan, E. Delhaize, Y. Yamamoto, An extracellular hydrophilic carboxy-terminal domain regulates the activity of *Ta*ALMT1, the aluminum-activated malate transport protein of wheat. *Plant J.* **64**, 47–55 (2010).

25. R. Dutzler, E. B. Campbell, M. Cadene, B. T. Chait, R. MacKinnon, X-ray structure of a ClC chloride channel at 3.0 Å reveals the molecular basis of anion selectivity. *Nature* **415**, 287–294 (2002).

26. O. S. Smart, J. G. Neduvelil, X. Wang, B. A. Wallace, M. S. P. Sansom, HOLE: A program for the analysis of the pore dimensions of ion channel structural models. *J. Mol. Graph.* **14**, 354–360 (1996).

27. W. Peng, W. Wu, J. Peng, J. Li, Y. Lin, Y. Wang, J. Tian, L. Sun, C. Liang, H. Liao, Characterization of the soybean *Gm*ALMT family genes and the function of *Gm*ALMT5 in response to phosphate starvation. *J. Integr. Plant Biol.* **60**, 216–231 (2018).

28. J. Jumper, R. Evans, A. Pritzel, T. Green, M. Figurnov, O. Ronneberger, K. Tunyasuvunakool, R. Bates, A. Žídek, A. Potapenko, A. Bridgland, C. Meyer, S. A. A. Kohl, A. J. Ballard, A. Cowie, B. Romera-Paredes, S. Nikolov, R. Jain, J. Adler, T. Back, S. Petersen, D. Reiman, E. Clancy, M. Zielinski, M. Steinegger, M. Pacholska, T. Berghammer, S. Bodenstein, D. Silver, O. Vinyals, A. W. Senior, K. Kavukcuoglu, P. Kohli, D. Hassabis, Highly accurate protein structure prediction with AlphaFold. *Nature* **596**, 583–589 (2021).

29. F. Malcheska, A. Ahmad, S. Batool, H. M. Müller, J. Ludwig-Müller, J. Kreuzwieser, D. Randewig, R. Hänsch, R. R. Mendel, R. Hell, M. Wirtz, D. Geiger, P. Ache, R. Hedrich, C. Herschbach, H. Rennenberg, Drought-enhanced xylem sap sulfate closes stomata by affecting ALMT12 and guard cell ABA synthesis. *Plant Physiol.* **174**, 798–814 (2017).

30. O. Pantoja, Recent advances in the physiology of ion channels in plants. *Annu. Rev. Plant Biol.* **72**, 463–495 (2021).

31. J. I. Schroeder, S. Hagiwara, Cytosolic calcium regulates ion channels in the plasma membrane of *Vicia faba* guard cells. *Nature* **338**, 427–430 (1989).

32. R. Hedrich, H. Busch, K. Raschke, Ca^{2+} and nucleotide dependent regulation of voltage dependent anion channels in the plasma membrane of guard cells. *EMBO J.* **9**, 3889–3892 (1990).

33. T. Vahisalu, H. Kollist, Y. F. Wang, N. Nishimura, W. Y. Chan, G. Valerio, A. Lamminmäki, M. Brosché, H. Moldau, R. Desikan, J. I. Schroeder, J. Kangasjärvi, SLAC1 is required for plant guard cell S-type anion channel function in stomatal signalling. *Nature* **452**, 487–491 (2008).

34. J. Negi, O. Matsuda, T. Nagasawa, Y. Oba, H. Takahashi, M. Kawai-Yamada, H. Uchimiya, M. Hashimoto, K. Iba, CO_2 regulator SLAC1 and its homologues are essential for anion homeostasis in plant cells. *Nature* **452**, 483–486 (2008).

35. S. Saji, S. Bathula, A. Kubo, M. Tamaoki, M. Kanna, M. Aono, N. Nakajima, T. Nakaji, T. Takeda, M. Asayama, H. Saji, Disruption of a gene encoding C4-dicarboxylate transporter-like protein increases ozone sensitivity through deregulation of the stomatal response in *Arabidopsis thaliana*. *Plant Cell Physiol.* **49**, 2–10 (2008).

36. D. Geiger, S. Scherzer, P. Mumm, A. Stange, I. Marten, H. Bauer, P. Ache, S. Matschi, A. Liese, K. A. S. S. Al-Rasheid, T. Romeis, R. Hedrich, Activity of guard cell anion channel SLAC1 is controlled by drought-stress signaling kinase-phosphatase pair. *Proc. Natl. Acad. Sci. U.S.A.* **106**, 21425–21430 (2009).

37. S. C. Lee, W. Lan, B. B. Buchanan, S. Luan, A protein kinase-phosphatase pair interacts with an ion channel to regulate ABA signaling in plant guard cells. *Proc. Natl. Acad. Sci. U.S.A.* **106**, 21419–21424 (2009).

38. B. Brandt, D. E. Brodsky, S. Xue, J. Negi, K. Iba, J. Kangasjärvi, M. Ghassemian, A. B. Stephan, H. Hu, J. I. Schroeder, Reconstitution of abscisic acid activation of SLAC1 anion channel by CPK6 and OST1 kinases and branched ABI1 PP2C phosphatase action. *Proc. Natl. Acad. Sci. U.S.A.* **109**, 10593–10598 (2012).

39. T. Maierhofer, M. Diekmann, J. N. Offenborn, C. Lind, H. Bauer, K. Hashimoto, K. A. S. Al-Rasheid, S. Luan, J. Kudla, D. Geiger, R. Hedrich, Site- and kinase-specific phosphorylation-mediated activation of SLAC1, a guard cell anion channel stimulated by abscisic acid. *Sci. Signal.* **7**, ra86 (2014).

40. Y.-N. Deng, H. Kashtoh, Q. Wang, G.-X. Zhen, Q. Li, L.-H. Tang, H.-L. Gao, C.-R. Zhang, L. Qin, M. Su, F. Li, X.-H. Huang, Y.-C. Wang, Q. Xie, O. B. Clarke, W. A. Hendrickson, Y.-H. Chen, Structure and activity of SLAC1 channels for stomatal signaling in leaves. *Proc. Natl. Acad. Sci. U.S.A.* **118**, e2015151118 (2021).

41. Y.-H. Chen, L. Hu, M. Punta, R. Bruni, B. Hillerich, B. Kloss, B. Rost, J. Love, S. A. Siegelbaum, W. A. Hendrickson, Homologue structure of the SLAC1 anion channel for closing stomata in leaves. *Nature* **467**, 1074–1080 (2010).

42. S. F. Altschul, T. L. Madden, A. A. Schäffer, J. Zhang, Z. Zhang, W. Miller, D. J. Lipman, Gapped BLAST and PSI-BLAST: A new generation of protein database search programs. *Nucleic Acids Res.* **25**, 3389–3402 (1997).

43. X.-H. Wang, M. Su, F. Gao, W. Xie, Y. Zeng, D. Li, X. Liu, H. Zhao, L. Qin, F. Li, Q. Liu, O. B. Clarke, S. M. Lam, G. Shui, W. A. Hendrickson, Y.-H. Chen, Structural basis for

activity of TRIC counter-ion channels in calcium release. *Proc. Natl. Acad. Sci. U.S.A.* **116**, 4238–4243 (2019).

44. D. N. Mastronarde, Automated electron microscope tomography using robust prediction of specimen movements. *J. Struct. Biol.* **152**, 36–51 (2005).

45. C. Wu, X. Huang, J. Cheng, D. Zhu, X. Zhang, High-quality, high-throughput cryo-electron microscopy data collection via beam tilt and astigmatism-free beam-image shift. *J. Struct. Biol.* **208**, 107396 (2019).

46. J. Zivanov, T. Nakane, B. O. Forsberg, D. Kimanius, W. J. H. Hagen, E. Lindahl, S. H. W. Scheres, New tools for automated high-resolution cryo-EM structure determination in RELION-3. *eLife* **7**, e42166 (2018).

47. A. Punjani, J. L. Rubinstein, D. J. Fleet, M. A. Brubaker, cryoSPARC: Algorithms for rapid unsupervised cryo-EM structure determination. *Nat. Methods* **14**, 290–296 (2017).

48. D. Asarnow, E. Palovcak, Y. F. Cheng, UCSF pyem v0.5 (2019); doi:10.5281/zenodo.3576630.

49. E. F. Pettersen, T. D. Goddard, C. C. Huang, G. S. Couch, D. M. Greenblatt, E. C. Meng, T. E. Ferrin, UCSF Chimera—A visualization system for exploratory research and analysis. *J. Comput. Chem.* **25**, 1605–1612 (2004).

50. S. Q. Zheng, E. Palovcak, J.-P. Armache, K. A. Verba, Y. Cheng, D. A. Agard, MotionCor2: Anisotropic correction of beam-induced motion for improved cryo-electron microscopy. *Nat. Methods* **14**, 331–332 (2017).

51. K. Zhang, Gctf: Real-time CTF determination and correction. *J. Struct. Biol.* **193**, 1–12 (2016).

52. K. Zhang, F. Sun, Gautomatch: An efficient and convenient gpu-based automatic particle selection program (2011); https://www2.mrc-lmb.cam.ac.uk/research/locally-developed-software/zhang-software/.

53. D. Liebschner, P. V Afonine, M. L. Baker, G. Bunkóczi, V. B. Chen, T. I. Croll, B. Hintze, L.-W. Hung, S. Jain, A. J. McCoy, N. W. Moriarty, R. D. Oeffner, B. K. Poon, M. G. Prisant, R. J. Read, J. S. Richardson, D. C. Richardson, M. D. Sammito, O. V Sobolev, D. H. Stockwell, T. C. Terwilliger, A. G. Urzhumtsev, L. L. Videau, C. J. Williams, P. D. Adams, Macromolecular structure determination using X-rays, neutrons and electrons: Recent developments in PHENIX. *Acta Crystallogr. D. Struct. Biol.* **75**, 861–877 (2019).

54. A. Kucukelbir, F. J. Sigworth, H. D. Tagare, Quantifying the local resolution of cryo-EM density maps. *Nat. Methods* **11**, 63–65 (2014).

55. P. Emsley, B. Lohkamp, W. G. Scott, K. Cowtan, Features and development of Coot. *Acta Crystallogr. D Biol. Crystallogr.* **66**, 486–501 (2010).

56. F. Gabler, S.-Z. Nam, S. Till, M. Mirdita, M. Steinegger, J. Söding, A. N. Lupas, V. Alva, Protein sequence analysis using the MPI bioinformatics toolkit. *Curr. Protoc. Bioinformatics* **72**, e108 (2020).

57. B. A. Barad, N. Echols, R. Y. R. Wang, Y. Cheng, F. Dimaio, P. D. Adams, J. S. Fraser, EMRinger: Side chain-directed model and map validation for 3D cryo-electron microscopy. *Nat. Methods* **12**, 943–946 (2015).

58. E. F. Pettersen, T. D. Goddard, C. C. Huang, E. C. Meng, G. S. Couch, T. I. Croll, J. H. Morris, T. E. Ferrin, UCSF ChimeraX: Structure visualization for researchers, educators, and developers. *Protein Sci.* **30**, 70–82 (2021).

59. G. Bi, M. Su, N. Li, Y. Liang, S. Dang, J. Xu, M. Hu, J. Wang, M. Zou, Y. Deng, Q. Li, S. Huang, J. Li, J. Chai, K. He, Y.-H. Chen, J.-M. Zhou, The ZAR1 resistosome is a calcium-permeable channel triggering plant immune signaling. *Cell* **184**, 3528–3541.e12 (2021).

60. I. Dreyer, J. L. Gomez-Porras, D. M. Riaño-Pachón, R. Hedrich, D. Geiger, Molecular evolution of slow and quick anion channels (SLACs and QUACs/ALMTs). *Front. Plant Sci.* **3**, 263 (2012).